2022 SCEC Final Report

Project Title:
Geodetic Imaging of Earthquakes, Fault Creep, Deformation, and Coastal Changes at the Southern Salton Sea over Two Decades

PI: Junle Jiang (University of Oklahoma, USA)

Total Award Period Covered: February 1, 2022 – January 31, 2023

Proposal Category: Individual Proposal, Integration and Theory

SCEC Research Priorities: P1.a, P1.b, P3.f.

Summary

The Imperial Valley region in Southern California straddles the transitional zone from the southern terminus of the San Andreas fault to a series of right-lateral faults and extensional structures that extend to the Imperial fault and across the US-Mexico border [*Elders et al.*, 1972; *Fuis et al.*, 1984; *Brothers et al.*, 2009] (Figure 1a). Earthquakes, seismic swarms, and transient fault creep are frequently documented in the region [*Hudnut*, 1989; *Meltzner et al.*, 2006; *Lohman and McGuire*, 2007; *Wei et al.*, 2015; *McGuire et al.*, 2015; *Tymofyeyeva et al.*, 2019]. Along with these tectonic processes, widespread agricultural activities and geothermal power plant operations occur south of the Salton Sea. The Salton Sea geothermal field (SSGF), situated within the Brawley seismic zone, has operated for over three decades. While some of the observed deformation and seismic swarms have been associated with aseismic faulting along larger, long-lived structures [*Lohman and McGuire*, 2007], it is suggested that the overall seismicity rates in the region correlate with, and are likely affected by, geothermal operations [*Brodsky and Lajoie*, 2013] and the observed surface displacement can be attributed to reservoir depletion [*Barbour et al.*, 2016]. High-resolution observations of ground displacement over time are key to addressing many questions related to the regional tectonic and anthropogenic processes.

With SCEC support in 2020–2021 (no cost extension to 2022), we have developed a multi-temporal InSAR analysis approach to extract deformation signals from high-quality pixels despite nearby ongoing land surface changes [*Jiang and Lohman*, 2021]. We derived high-resolution surface displacement history for the Imperial Valley from Sentinel-1 data over 2015–2019 (Figure 1b) and Envisat data over 2003–2010. The observations allow us to better investigate the respective roles of faulting and fluid injection/production in the SSGF. Our modeling efforts suggest that anthropogenic reservoir deformation can only partly explain the relative subsidence and uplift over smaller spatial scales, while the regional tectonic motion likely causes the larger-scale (and potentially some smaller-scale) subsidence observed by InSAR. In addition, we have collaborated with USGS researchers to use our InSAR products to study the fault creep and reservoir deformation processes at the North Brawley geothermal field (*Materna et al.*, 2022).

In this project, we have extended our InSAR time series analysis in this region over two decades, including recent seismic swarms in June 2021 at the Salton Sea geothermal field. The new InSAR observations reveal the weeks-long transient deformation associated with the earthquake swarms and fault slip, enabling a comparison between the 2021 and 2005 seismic swarms. We have also trained a Ph.D. student in quantifying the effects of layered hydromechanical and elastic rock properties on time-dependent poroelastic deformation and pore pressure history in geothermal fields such as the SSGF. The simplified three-dimensional models allow us to simulate reservoir behavior more accurately due to fluid injection/production and better infer the subsurface reservoir properties from surface geodetic observations. These models also improve the estimates of subsurface stress changes over time, which we plan to explore in the future. These observational and modeling efforts will further help distinguish different physical processes and understand the links between deformation and seismicity in the region.

Results: InSAR Observations of Decadal Deformation and 2021 Swarm

The main challenges facing geophysical studies of the Salton Trough using InSAR are the decorrelation of radar signals in agricultural fields and coherent signals that are not related to deformation, e.g., those due to land surface/vegetation changes and soil moisture variability [*Gabriel et al.*, 1989]. Previously, we developed an InSAR time series approach to extract temporally coherent signals in the Imperial Valley, California [*Jiang and Lohman*, 2021]. We use SAR imagery for ~100 dates over 2015–2019 from the descending and ascending orbits of the European Space Agency (ESA) Sentinel-1a/b satellite. We derived the line-of-sight (LOS) displacement time series and linear secular velocity estimates for the region.

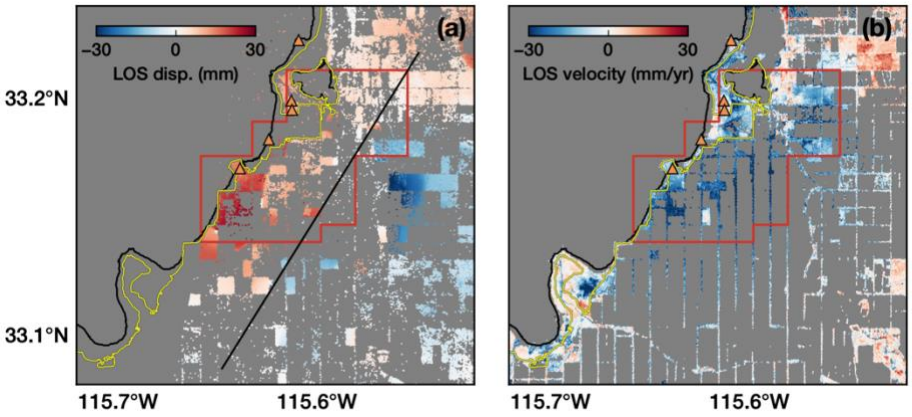

Figure 1. InSAR observations of the Salton Sea Geothermal Field (SSGF). **(a)** LOS displacement for the 2005 swarm (Envisat descending track 84) with pixels of coherence>0.5. **(b)** LOS secular velocity for 2015–2019 (Sentinel-1 descending track 173). The noisy areas (gray) are masked based on pixel coherence history. The SSGF boundary is outlined in red. Salton Buttes are orange triangles. The coastlines in 2001 (yellow) and 2016 (black) are shown.

The secular velocity field within the SSGF features negative LOS rates of ~ 20 mm/yr over a broad region in both tracks (suggesting a predominantly vertical subsidence rate of ~25 mm/yr) over spatial scales of ~20 km, with some variations over small scales of ~1 km (Figure 1). The existing GPS network is too sparse to resolve the spatial complexity of the deformation field. The subsidence patterns appear to extend beyond the boundary of the geothermal production field, suggesting that larger-scale tectonic processes or fluid flow are likely responsible for at least part of the observed deformation. To compare observations in recent years with earlier periods [*Lohman and McGuire*, 2007], we apply a similar InSAR approach to the Envisat data (2003–2010), which tends to have sparser temporal coverage and poorer data quality. Nonetheless, one Envisat interferogram in September 2005 (Figure 1) clearly captures ground deformation associated with the 2005 seismic swarm.

We processed InSAR data that span the period for the 2021 seismic swarm sequence, with the largest earthquake being a magnitude 5.3 strike-slip event and most events small in magnitude (M<4) and relatively shallow (Figure 2). Like the 2005 swarm, the 2021 swarm exhibits numerous clusters and lineation, as may be expected for the complex tectonic setting south of the Salton Sea [*Brothers et al.*, 2009]. The 6-day interferogram (2021/5/31–2021/6/6) from the descending track 173 features large areas that have decorrelated InSAR signals due to agriculture; however, we can still observe several fringes indicating high spatial gradients in displacements, likely associated with the uplift and subsidence across an extensional fault structure [*Brothers et al.*, 2009; *Lohman and McGuire*, 2007]. The suspected fault geometry (dashed line in Figure 2) appears offset from the seismicity catalog from SCEDC, potentially due to the inaccuracy in the preliminary earthquake locations. InSAR observations also reveal the continuous changes of the coastline of the Salton Sea, due to decreasing lake level. Much of the onshore areas tend to exhibit high InSAR coherence and record ground deformation signals.

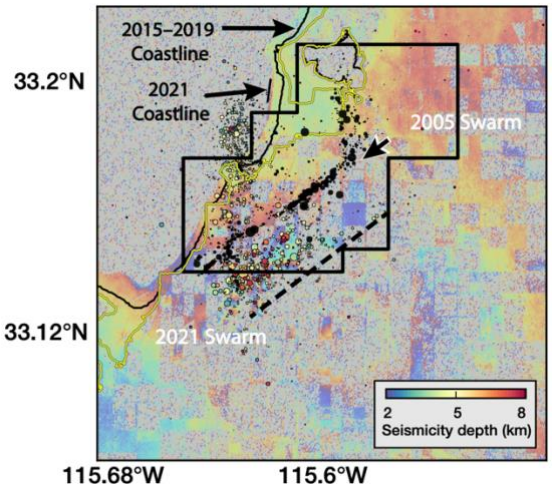

Figure 2. InSAR observations of the seismic swarm in June 2021. An interferogram of Sentinel-1 descending track 173 is shown in the background. Pixels with coherence below 0.5 are masked. The dashed line represents the approximate fault geometry based on uplifted and subsided areas. The 2005 swarm is shown as black dots (*Hauksson et al.*, 2012). The 2021 earthquake swarms (from the SCEDC catalog) are colored by event depths; the size of earthquakes scale with their magnitudes. The coastlines in 2015–2019 and 2021 are indicated by arrows.

Results: Hydromechanical Modeling of Heterogeneous Geothermal Fields

The InSAR observations of ground deformation history can provide unique constraints on the geothermal reservoir properties in the Imperial Valley. In our earlier work, we used simple models of subsurface volumetric sources in a homogeneous half-space [*Segall*, 1985], along with information on wellhead depths and the total amount of fluid production and injection at individual well sites within the SSGF to calculate the predicted combined surface displacements. In this project, we have supported and trained a Ph.D. student, Ganiyat Shodunke, to quantify the deformation characteristics of a heterogeneous geothermal reservoir subject to injection/production, motivated by new observations from the SSGF and Brawley Geothermal Field [*Jiang and Lohman*, 2021; *Materna et al.*, 2022].

We have created three-dimensional finite-element models for a three-layered geothermal field (Figure 3). These models feature a shallow sedimentary rock or caprock layer (thickness of h_1) overlying the shallower and deeper geothermal reservoirs (thickness of h_2 and h_3, respectively). We have designed a suite of homogeneous reservoir scenarios (e.g., different permeability/porosity/elastic moduli) and heterogeneous reservoir scenarios (e.g., compaction-induced porosity variations and different contrasts in caprock-reservoir properties). The porosity and hydraulic conductivity of simulated geothermal systems range from 2% to 40% and 10^{-6} m/s to 10^{-10} m/s, respectively. In these scenarios, we characterize the time evolution and final amplitude of poroelastic deformation (Figure 3) and estimate how the approximations for homogeneous structures can bias the inference of the depth and strength of the pressurizing sources.

Our results suggest the influence of layered heterogeneity on poroelastic deformation and pore pressure modeling is significant, with steady-state rates of deformation and pressure change differing by up to 40% compared to a homogeneous model scenario. We show that permeability has a greater influence than compaction-influenced porosity on the magnitude and time evolution of subsidence and pore pressure in a geothermal setting. We have presented these results at the AGU Fall Meeting and a regional workshop [*Shodunke et al.*, 2022, 2024] and are currently preparing a manuscript for publication in a peer-reviewed journal.

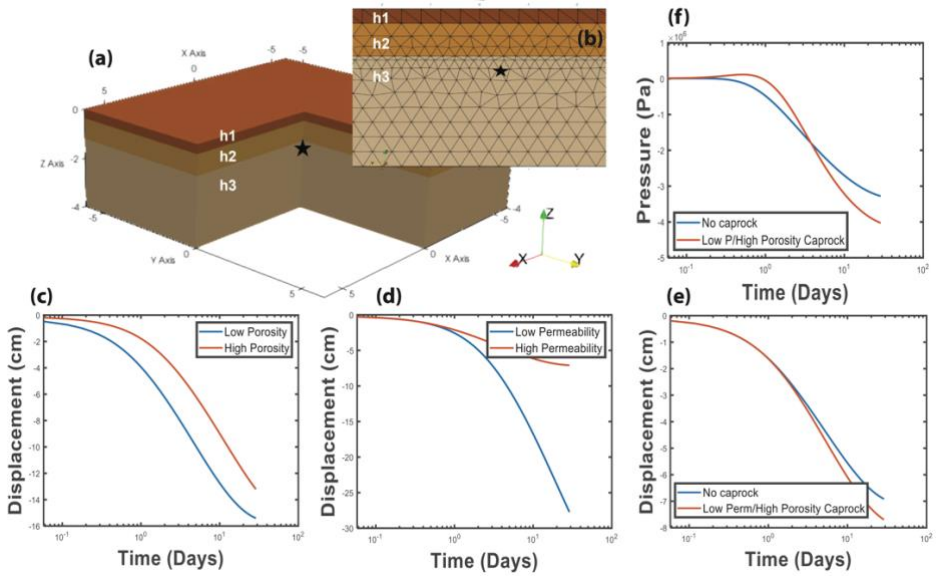

Figure 3. Poroelastic deformation at geothermal fields. **(a)** A three-dimensional finite-element (FE) model for a three-layered structure (thicknesses of h_1, h_2, and h_3). **(b)** A cross-section view of FE meshes and production well location (star). **(c–e)** Comparisons of different models illustrate the effect of (c) porosity (homogeneous models), (d) permeability (homogeneous models), and (e) low-permeability/high-porosity caprock (heterogeneous models) on the time evolution of surface deformation. Panel (f) shows near-surface pore pressure evolution for models in (e).

Our ongoing work involves calculating the combined deformation signals due to concurrent operations at multiple wells. More accurate models of reservoir deformation should help us further isolate the short- and long-wavelength geodetic signals and refine models of fault movement along the Obsidian Buttes fault [*Barbour et al.*, 2016] and potentially other parallel structures [*Brothers et al.*, 2009].

Related Presentations & Publications

Jiang, J., & Lohman, R. B. (2021). Coherence-guided InSAR deformation analysis in the presence of ongoing land surface changes in the Imperial Valley, California. *Remote Sensing of Environment*, *253*, 112160.

Materna, K., Barbour, A., Jiang, J., & Eneva, M. (2022). Detection of aseismic slip and poroelastic reservoir deformation at the North Brawley Geothermal Field from 2009 to 2019. *Journal of Geophysical Research: Solid Earth*, *127*(5), e2021JB023335.

Shodunke, G. O., Jiang, J., and Bodunde, S., Investigating the Effects of Permeability and Porosity on Reservoir Deformation and Pore Pressure Evolution at Geothermal Fields, AGU Fall Meeting, Chicago, IL, December 2022.

Shodunke, G. O., Jiang, J., and Bodunde, S., Hydromechanical Impacts of Rock Layer Heterogeneity on Poroelastic Deformation and Fluid Flow in Geothermal Fields: A 3D Finite-Element Modeling Approach, SEG/SPE/SPWLA Workshop, Norman, OK, March 2024.

References

Barbour, A. J., Evans, E. L., Hickman, S. H., & Eneva, M. (2016). Subsidence rates at the southern Salton Sea consistent with reservoir depletion. *Journal of Geophysical Research: Solid Earth*, 121, 5308–5327.

Brodsky, E. E., & Lajoie, L. J. (2013). Anthropogenic Seismicity Rates and Operational Parameters at the Salton Sea Geothermal Field. *Science*, *341*, 543–546.

Brothers, D. S., Driscoll, N. W., Kent, G. M., Harding, A. J., Babcock, J. M., & Baskin, R. L. (2009). Tectonic evolution of the Salton Sea inferred from seismic reflection data. *Nature Geoscience*, *2*, 581–584.

Elders, W. A., Rex, R. W., Robinson, P. T., Biehler, S., & Meidav, T. (1972). Crustal Spreading in Southern California: The Imperial Valley and the Gulf of California formed by the rifting apart of a continental plate. *Science*, *178*, 15–24.

Eneva, M., Adams, D., Falorni, G., Novali, F., & Hsiao, V. (2014). Surface Deformation at the Salton Sea Geothermal Field from High-Precision Radar Interferometry. In *Geothermal Resources Council Transactions* (pp. 991–999). volume 38.

Fuis, G. S., Mooney, W. D., Healy, J. H., McMechan, G. A., & Lutter, W. J. (1984). A seismic refraction survey of the Imperial Valley Region, California. *Journal of Geophysical Research: Solid Earth*, *89*, 1165–1189.

Gabriel, A. K., Goldstein, R. M., & Zebker, H. A. (1989). Mapping small elevation changes over large areas: Differential radar interferometry. *Journal of Geophysical Research: Solid Earth*, *94*, 9183–9191. doi:10/frsz8s.

Hauksson, E., Yang, W., & Shearer, P. M. (2012). Waveform relocated earthquake catalog for Southern California (1981 to June 2011). *Bulletin of the Seismological Society of America*, 102, 2239–2244.

Hudnut, K., Seeber, L., Rockwell, T., Goodmacher, J., Klinger, R., Lindvall, S., & McElwain, R. (1989). Surface ruptures on cross-faults in the 24 November 1987 Superstition Hills, California, earthquake sequence. *Bulletin of the Seismological Society of America*, *79*, 282–296.

Jiang, J., & Lohman, R. B. (2021). Coherence-guided InSAR deformation analysis in the presence of ongoing land surface changes in the Imperial Valley, California. *Remote Sensing of Environment*, *253*, 112160.

Lohman, R. B., & McGuire, J. J. (2007). Earthquake swarms driven by aseismic creep in the Salton Trough, California. *Journal of Geophysical Research: Solid Earth*, 112.

Ross, Z. E., Trugman, D. T., Hauksson, E., & Shearer, P. M. (2019). Searching for hidden earthquakes in Southern California. *Science*, *364*(6442), 767-771.

Tymofyeyeva, E., Fialko, Y., Jiang, J., Xu, X., Sandwell, D., Bilham, R., et al. (2019). Slow slip event on the southern San Andreas fault triggered by the 2017 *Mw*8.2 Chiapas (Mexico) earthquake. *Journal of Geophysical Research: Solid Earth*, 124, 9956– 9975.

McGuire, J. J., Lohman, R. B., Catchings, R. D., Rymer, M. J., & Goldman, M. R. (2015). Relationships among seismic velocity, metamorphism, and seismic and aseismic fault slip in the Salton Sea Geothermal Field region. *Journal of Geophysical Research: Solid Earth*, 120, 2600–2615.

Meltzner, A. J., Rockwell, T. K., & Owen, L. A. (2006). Recent and Long-Term Behavior of the Brawley Fault Zone, Imperial Valley, California: An Escalation in Slip Rate? *Bulletin of the Seismological Society of America*, *96*, 2304–2328.

Wei, S., Avouac, J. P., Hudnut, K. W., Donnellan, A., Parker, J. W., Graves, R. W., ... & Eneva, M. (2015). The 2012 Brawley swarm triggered by injection-induced aseismic slip. *Earth and Planetary Science Letters*, *422*, 115-125.